ACS APPLIED ENERGY MATERIALS

www.acsaem.org Article

Zinc Oxide Coated Carbon Dot Nanoparticles as Electron Transport Layer for Inverted Polymer Solar Cells

Wensheng Zhao, Lingpeng Yan,* Huimin Gu, Zerui Li, Yaling Wang, Qun Luo, Yongzhen Yang,* Xuguang Liu, Hua Wang, and Chang-Qi Ma*

Cite This: *ACS Appl. Energy Mater.* 2020, 3, 11388−11397 Read Online

ACCESS | Metrics & More | Article Recommendations | Supporting Information

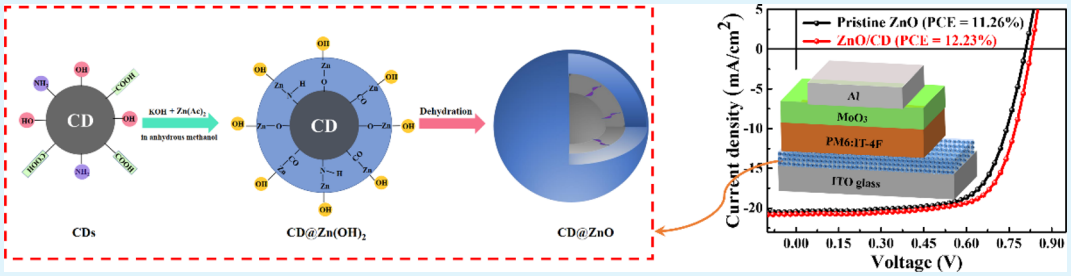

ABSTRACT: Interface engineering is a powerful tool to improve the performance of polymer solar cells (PSCs), and zinc oxide (ZnO) is a significant interfacial material for PSCs. However, ZnO is easy to agglomerate, which leads to low charge conductivity and poor stability; moreover, the hydroxyl groups on its surface also lead to a large number of defects, which restricts the application of ZnO. In order to improve the dispersion stability of ZnO nanoparticles and inhibit its surface defects, ZnO coated carbon dot (CD@ZnO) nanoparticles are first synthesized by direct particle precipitation. The introduced CD induces and participates in the growth of ZnO crystal. As a result, CD@ZnO nanoparticles show better colloidal stability, wider energy band gap, and fewer surface defects, which enhances the exciton extraction and restrains the charge recombination at the interface of the active layer and electron transport layer (ETL) of PSCs. Therefore, the device based on poly[[4,8-bis[5-(2-ethylhexyl)-4-fluoro-2-thienyl]benzo[1,2-*b*:4,5-*b*′]dithiophene-2,6-diyl]-2,5-thiophenediyl[5,7-bis(2-ethylhexyl)-4,8-dioxo-4*H*,8*H*-benzo[1,2-*c*:4,5-*c*′]dithiophene-1,3-diyl]-2,5-thiophenediyl]:3,9-bis(1-oxo-2-methylene-3-(1,1-dicyanomethylene)-5,6-difluoroindanone)-5,5,11,11-tetrakis(4-*n*-hexylphenyl)-dithieno[2,3d:2′,3′d′]-*s*-indaceno[1,2-*b*:5,6-*b*′]dithiophene with CD@ZnO as ETL exhibits a greatly strengthened power conversion efficiency of 12.23% compared to 11.26% of the reference device. Meanwhile, the CD@ZnO ETL also achieved a big performance boost in fullerene-based solar cells. This work offers an available method using CDs to modify ZnO for highly efficient PSCs.

KEYWORDS: *polymer solar cells, ZnO, carbon dot, core−shell composites, electron transport layer*

1. INTRODUCTION

Polymer solar cells (PSCs) are considered as a promising new energy technology for advantages such as light weight, flexibility, roll-to-roll fabrication, and portable devices.[1] Recently, the highest power conversion efficiency (PCE) of PSCs has exceeded 18%,[2] which shows great commercial prospect of PSCs. To further ameliorate the PCE and stability of PSCs is beneficial to realizing their commercialization. So far, many strategies have been used to make new breakthroughs in the PCE of PSCs, such as molecular design of novel materials,[1] morphology optimization of active layer,[3] and interface engineering.[4] Among these strategies, interfacial engineering has dual functions, which can simultaneously enhance the PCE and stability of PSCs.[4]

Compared with conventional PSCs, the inverted PSCs using metal oxide as the electron transport layer (ETL) demonstrate a better long-term stability.[5] ZnO has been extensively used as ETL in inverted PSCs because of its high charge conductivity, matched energy level, air stability, high transmittance under sunlight, and easy preparation.[6,7] In general, there are two main ways to synthesize ZnO used in PSCs: the sol−gel method[8] and direct particle precipitation method.[9] In the preparation of nanometer ZnO by sol−gel method, the precursor solution needs to be calcined at about 200 °C to obtain the ZnO thin film. High temperature process is not conducive to the industrial production of PSCs, especially for the printing preparation of flexile large-area devices.[10] Moreover, there are many crystal defects in a ZnO layer, such as oxygen vacancy and excess hydroxyl groups, which are considered to be the

Received: September 20, 2020
Accepted: October 21, 2020
Published: November 4, 2020

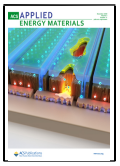

https://dx.doi.org/10.1021/acsaem.0c02323
ACS Appl. Energy Mater. 2020, 3, 11388−11397

electron trap sites causing poor electron mobility of ZnO thin film.[11] In comparison, the preparation of ZnO by direct particle precipitation does not require high temperature calcination, which can meet the demand of PSCs for industrial production, demonstrating great application potential. However, the ZnO prepared by direct particle precipitation is easy to reunite. In addition, the "light soaking" phenomenon, which is caused by the defects on the surface and inside of ZnO, can worsen the PCE of PSCs.[12] Therefore, the modification of ZnO synthesized by direct particle precipitation is of great significance for improving the PCE of PSCs.

A great deal of work has been done to suppress the defects of ZnO synthesized by direct particle precipitation, and it can be roughly divided into two categories. The first is physical modification, that is, mixing simple organic molecules with ZnO or spin coating organic molecules above ZnO film to form a double ETL. For example, poly[(9,9-bis(3′-(*N*,*N*-dimethylamino)propyl)-2,7-fluorene)-*alt*-2,7-(9,9-dioctyl)-fluorene] (PFN),[13] bis(trifluoromethane)sulfonimide lithium salt (Li-TFSI),[14] and tetrafluoroterephthalic acid (TFTPA)[15] were doped into ZnO ETL, which can increase the dissociation of excitons and reduce the exciton recombination at the active layer/ETL interface, resulting in enhanced device performance. Besides, double ETLs, such as ZnO/Al,[16] ZnO/PFN,[13] and ZnO/ethoxylated polyethyleneimine (PEIE),[17] were used to passivate the ZnO surface defects, so as to achieve higher PCE and better stability of PSCs.

Another kind of modification is chemical modification, including surface grafting and chemical doping. For example, Wei et al.[18] grafted 3-aminopropyltrimethoxysilane (APTMS) onto the surface of ZnO, which effectively reduces the surface-adsorbed oxygen groups and enhances the electron transfer rate of ZnO, resulting in suppressed "light-soaking". Also many other organic molecules have been used to modify ZnO surface, such as glutamic acid (Gly)[19] and 2-(2-(2-methoxyethoxy)ethoxy)ethylundec-10-enyl malonate C-60 (EEMC).[20] In addition, Ling et al.[21] modified ZnO with various alkali metal halides (LiF, LiCl, and LiBr), which also increases the electron transport capacity of ZnO and suppresses the "light soaking". Moreover, various metal elements were doped into ZnO, such as Al^{3+},[22,23] Li^{+},[24,25] Ga^{2+},[26] Sn^{4+},[27] and Cs^{2+},[28] since metal doping could effectively improve the electrical conductivity of ZnO.

Currently, carbon dots (CDs) have also been used to modify ZnO,[29−31] owing to their excellent photoelectric properties,[32] tunable optical and electronic properties,[33] photochemical stability,[34] and abundant surface functional groups.[35] For example, Lin et al.[29] used rationally designed CDs with amino groups as an interfacial modification on ZnO films. As a result, the work function and roughness of ZnO have been decreased and the transport of photogenerated charge carriers has also been facilitated, hence greatly improving device performance. Wang et al.[31] overcame the light-soaking effect in PSCs by using N, S-doped CDs as efficient surface modifier for ZnO. It can be seen from the above reports that CDs are mainly used to physically modify ZnO on its surface. The resulting composite structure is poor in stability.

Herein, ZnO-coated CD (CD@ZnO) nanoparticles were synthesized by doping CDs in situ during the synthesis of ZnO by direct particle precipitation and used as ETL in PSCs. Compared with the reported physical modification of ZnO by CDs, the synthesis of CD@ZnO is a one-step in situ chemical process featuring more stable structure and simpler operation. The introduction of CDs not only effectively passivate the external and internal crystal defects of pristine ZnO but also inhibited agglomeration of ZnO. Finally, the inverted PSCs based CD@ZnO ETL displayed markedly improved PCE with respect to those with a pristine ZnO ETL. These excellent properties of CD@ZnO ETLs afford a new opportunity for higher performance PSCs.

2. EXPERIMENTAL SECTION

2.1. Materials. CDs were synthesized from citric acid (CA) and ethylenediamine (EDA) through hydrothermal reaction as reported by Wang et al.[31] Zinc acetate dehydrate ($Zn(OAc)_2$ (99.999%)), methanol (99%), and KOH (85%) were purchased from Alfa Aesar. Poly(3-hexylthiophene) (P3HT, M_n = 5.0 × 10^4 g mol^{-1}), [6,6]-diphenyl-C_{62}-bis(butyric acid methyl ester) (bis-$PC_{61}BM$), poly[[4,8-bis[5-(2-ethylhexyl)-4-fluoro-2-thienyl]benzo[1,2-*b*:4,5-*b*′]-dithiophene-2,6-diyl]-2,5-thiophenediyl[5,7-bis(2-ethylhexyl)-4,8-dioxo-4*H*,8*H*-benzo[1,2-*c*:4,5-*c*′]dithiophene-1,3-diyl]-2,5-thiophene-diyl] (PM6), and 3,9-bis(1-oxo-2-methylene-3-(1,1-dicyanomethylene)-5,6-difluoroindanone)-5,5,11,11-tetrakis(4-*n*-hexylphenyl)-dithieno[2,3-*d*:2′,3′-*d*′]-*s*-indaceno[1,2-*b*:5,6-*b*′]dithiophene (IT-4F) were bought from Solarmer Materials Inc. (Beijing).

2.2. Synthesis of ZnO and CD@ZnO Nanoparticles. Pristine ZnO nanoparticles were prepared through a typical direct particle precipitation method reported in the literature.[9] However, the preparation method of CD@ZnO is different. The specific preparation steps are as follows. First, dissolve $Zn(OAc)_2$ (1.48 g, 6.7 mmol) in methanol and keep stirring and heat the solution to 63 °C. Then, a methanol solution of CDs (0%, 0.5%, 1%, 2%, 3%) and KOH (0.74 g, 11.5 mmol) was added to the $Zn(OAc)_2$ solution at a constant speed within 10 min. The doping ratio of CDs was determined by the ratio of the mass of doped CDs to the theoretical formation mass of ZnO. It should be noted that in the pristine ZnO preparation process, the solution began to precipitate in 1.5 h after KOH was added dropwise. However, after the introduction of CDs, the time of sample precipitation decreases as the proportion of CDs increases. The precipitation time of the samples doped with 0.5%, 1%, 2%, and 3% CDs were 1.4 h, 1 h, 50 min, and 30 min, respectively. The reaction phenomenon obviously proves that the introduced CDs induced the formation of ZnO nanoparticles. After about 2 h of reaction, stop heating and stirring. After leaving the reaction product stand for 2 h and removing the supernatant, the precipitate was washed twice with methanol. Finally, the CD@ZnO nanoparticles were centrifuged and strongly ultrasonically dispersed in methanol to obtain the CD@ZnO ink.

2.3. Preparation of Inverted PSCs. All PSCs with a configuration of ITO/ZnO(CD@ZnO)/active layer/MoO_3/Al were prepared. After ultrasonic cleaning with glass cleaner, acetone, and isopropanol, ITO glasses were treated with ozone under ultraviolet light for 30 min. After that, an ETL (ZnO or CD@ZnO) was spin-coated on the ITO substrate at 2000 rpm for 60 s and then annealed at 120 °C on the thermal platform for 10 min. After that, the active layers (PM6:IT-4F and P3HT:bis-PCBM) were deposited on ZnO or CD@ZnO ETL films. In particular, for the PM6:IT-4F devices, the solution of PM6 and IT-4F (1:1 (w/w), 20 mg/mL in chlorobenzene (containing 0.5 vol % DIO)) was spin-coated on the ETLs for 30 s at 2200 rpm. After that, the as-prepared layers were annealed for 15 min on the thermal platform with 150 °C. Besides, for the P3HT:bis-PCBM devices, the mixture solution of P3HT and bis-$PC_{61}BM$ (1:1.2 (w/w), 40 mg/mL in dichlorobenzene) was spin-coated on the ETLs at 600 rpm for 60 s. Next, the as-prepared films were put into covered Petri dishes in the glovebox for 2 h and annealed for 10 min on the thermal platform at 125 °C. Finally, fully covered MoO_3 (10 nm) and patterned Al (100 nm) were vapor-deposited on the active layer at 1 × 10^{-4} Pa.

2.4. Characterization. *2.4.1. Characterization of CD@ZnO.* The high resolution transmission electron microscopy (HRTEM) and energy-dispersive X-ray spectroscopy (EDX) measurements of CDs, ZnO, and CD@ZnO were performed by a Tecani G2 F20 S-Twin

https://dx.doi.org/10.1021/acsaem.0c02323
ACS Appl. Energy Mater. 2020, 3, 11388−11397

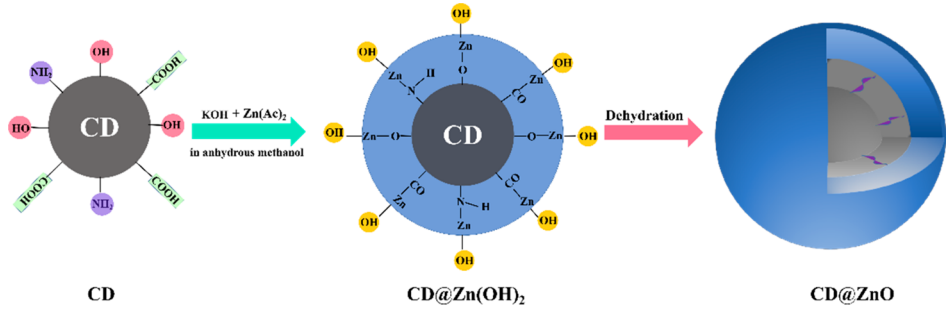

Figure 1. Synthesis schematic diagram of CD@ZnO nanoparticles.

field emission electron microscope. Ultraviolet photoelectron spectroscopy (UPS) and X-ray photoelectron spectroscopy (XPS) measurements were recorded on a PHI 5000 Versa Probe III X-ray photoelectron spectroscope. A BRUKER TENSOR 27 spectrometer was utilized to conduct Fourier transform infrared (FT-IR) spectroscopy analysis. X-ray diffraction (XRD) patterns were tested on a Rigaku D/max-2500. The thermal stability of pristine ZnO and CD@ZnO were characterized by a German NETZSCH TG209F3 thermogravimetry (TG) analyzer, operating in argon atmosphere from 100 to 900 °C with heating rate of 10 °C/min. A Lamada 750 UV/vis/NIR spectrophotometer (PerkinElmer) and a Horiba Fluoromax-4 spectrometer were used to test the ultraviolet−visible (UV−vis) absorption and photoluminescence (PL) spectra, respectively. The ζ electromotive potential of pristine ZnO and CD@ZnO nanoparticles was recorded by dynamic light scattering (DLS) using a Malvern granulometer (Zetasizer Nano).

2.4.2. Characterization of Inverted PSCs. Current density−voltage ($J-V$) curves of unencapsulated PSCs were measured in a N_2-filled glovebox illuminated with a solar simulator (ss150 solar simulator, Zolix), and a Keithley 2400 source meter was used to record the experimental data. External quantum efficiency (EQE) spectra were carried out with a solar cell spectra response measurement system where a tungsten halogen lamp (150 W, Osram 64610) is used as a probe light and a monochromator (Zolix, Omni-λ300) is used to select light wavelength. In addition, the $I-V$ converter was used to record the response of the device.

3. RESULTS AND DISCUSSION

3.1. CD@ZnO Microstructure and Properties. The synthesis of CD@ZnO belongs to in situ chemical doping, and Figure 1 shows the possible formation mechanism. CDs are mixed with KOH and added to the reaction system in the early stage. The phenomenon during experimental process proves that the introduced CDs induce and participate in the formation of CD@ZnO nanoparticles (section 2.2). By combination of the experimental phenomena and subsequent characterization results (vide infra), the formation mechanism of CD@ZnO is speculated as follows. In the initial stage, $Zn(Ac)_2$ reacts with KOH to form $Zn(OH)_2$. Then, since the surface of CDs are rich in −OH, −COOH, and $-NH_2$,[36] it is easy for CDs to undergo dehydration reaction with $Zn(OH)_2$ to connect together, which can be confirmed in following HRTEM, XPS, and FT-IR characterizations (vide infra). Finally, the $Zn(OH)_2$ on the surface of CD undergoes dehydration and condensation reactions, and finally a core−shell structure with ZnO coated on the surface of CD is formed.

The microstructures of CD@ZnO synthesized with different proportion of CDs are illustrated in Figure 2. It is obviously seen that the size of CDs is about 2−3 nm (Figure 2a). The surface of CDs is rich in various oxygen-containing functional groups, which makes them have good dispersibility. The size of

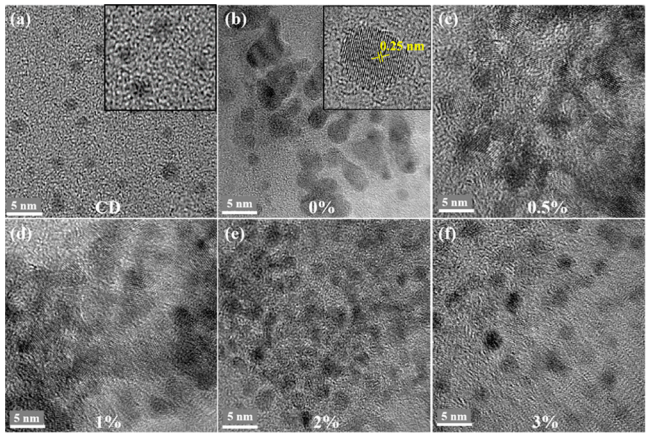

Figure 2. HRTEM images of (a) CDs, (b) pristine ZnO, CD@ZnO nanoparticles with different ratios of CDs (panels c, d, e, f represent 0.5%, 1%, 2%, 3%, respectively). The inset in (a) and (b) is the HRTEM image of CDs amorphous structure and ZnO lattice, respectively.

pristine ZnO is about 3−5 nm (Figure 2b), and the ZnO agglomerates seriously, forming clusters such that the particle size is about 5−8 nm. While different concentration of CDs are doped, the particle size of CD@ZnO increases slightly, and its size is about 5−8 nm. It is worth pointing out that as the amount of CDs increases (Figure 2b−f), the agglomeration of ZnO decreases. Obviously, chemical doping of CDs improves the monodispersity of CD@ZnO nanoparticles and improves the film-forming properties of CD@ZnO. In addition, the inset of Figure 2a shows that CDs have amorphous structure without lattice structure[31] and the inset of Figure 2b shows the structure of pristine ZnO in which the lattice spacing of ZnO is 0.25 nm, corresponding to (101) crystal plane.

Figure 3a shows the HRTEM images of CD@ZnO with 2% CDs doping content. In the figure, the core−shell structure of ZnO coated CD can be clearly distinguished. The diameter of the CD core is about 3 nm, with 1.8 nm in thickness of the ZnO shell, which confirms the previous mechanism hypothesis in Figure 1. Furthermore, the elemental analysis of the CD@ZnO (2%) was also carried out under HRTEM (Figure 3b−f). The EDX mapping image of CD@ZnO shows that Zn, O, and N are homogeneously distributed in the CD@ZnO nanoparticles. The content of ZnO nanoparticles can be confirmed by the determination of O and Zn elements. The surfaces of CDs contain amino groups, so the uniform distribution of the N element in ZnO further proves the composite structure of CD@ZnO. The above results rationalize the formation mechanism of CD@ZnO in Figure 1.

https://dx.doi.org/10.1021/acsaem.0c02323
ACS Appl. Energy Mater. 2020, 3, 11388−11397

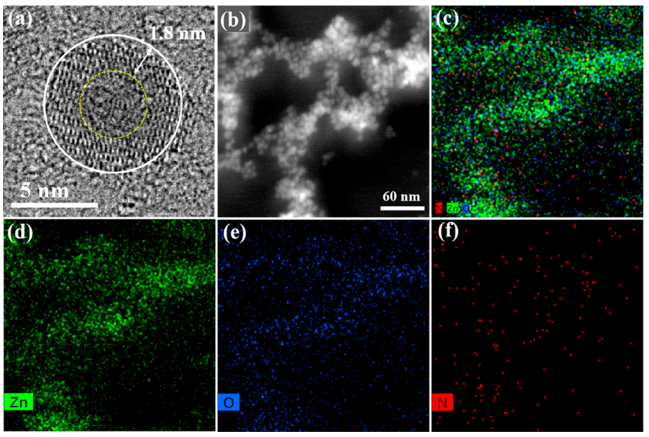

Figure 3. HRTEM images of (a) CD@ZnO nanoparticles with 2% CDs and (b, c) elemental analysis of (d) Zn, (e) O, (f) N elements in CD@ZnO.

XPS and FT-IR characterization was utilized to analyze the elements composition and chemical structure of CD@ZnO. Figure 4a shows the Zn $2p^{3/2}$ XPS spectra of as-prepared ZnO and CD@ZnO. As can be seen in Figure 4a, the binding energy of Zn $2p^{3/2}$ of pristine ZnO is located at 1021.2 eV, which corresponds to Zn−O bonds.[11,37] After doping with CDs, the maximum of the Zn $2p^{3/2}$ peak shifts toward higher binding energy. When the doping content is 3%, the XPS peak offset is the greatest and the binding energy of Zn $2p^{3/2}$ is located at 1021.9 eV, with an offset of 0.7 eV. It can be confirmed that the electronic states of ZnO in CD@ZnO are similar to those in ZnO−C_{60}[38] or Al-doped ZnO,[39] which indicates the formation of Zn−O−C bonds in CD@ZnO. Moreover, the N 1s signal at 399.9 eV is detected for CD@ZnO sample[31] (as shown in Figure S1), which further proves the formation of the composite of CDs and ZnO during the reaction. Figure 4b illustrates the FT-IR spectra of pristine ZnO and CD@ZnO. The bands at 420−600 cm^{-1} and 650−710 cm^{-1} for both samples correspond to the Zn−O vibration.[40−42] In addition, the Zn−N band is detected at 605−630 cm^{-1} for CD@ZnO,[41] and the band intensity increases with the increase of CDs doping ratio. The results indicate that the $-NH_2$ on the surface of CDs participates in the formation of ZnO by chemically bonding CDs onto ZnO.

The crystalline structure of CD@ZnO nanoparticles with different doping concentration of CDs was characterized by XRD pattern, as shown in Figure 4c. Pristine ZnO exhibits a series of typical characteristic peaks with 2θ at 31.8°, 34.4°, 36.3°, 47.5°, 56.6°, 62.9°, and 68.0°, which is referred to the (100), (002), (101), (102), (110), (103), and (112) crystal planes of ZnO with a hexagonal Wurtzite lattice, respectively.[43] The diffraction peaks of CD@ZnO are consistent with those of pristine ZnO, but the intensity of the diffraction peaks decreases. This means that the introduction of CDs to synthesize CD@ZnO nanoparticles does not change the crystal structure of ZnO but makes the ZnO shell thinner, which is consistent with the TEM results (Figure 2).

The TG analysis of ZnO and CD@ZnO is shown in Figure 4d. In the initial stage (100−250 °C), both samples show a little weight loss, which is mainly caused by the removal of water and impurities in samples. After that, both samples show a rapid weight loss process. Pristine ZnO decomposes at 250−500 °C, and the final weight loss rate is 7.4%. On the other hand, CD@ZnO decomposes at 250−800 °C, and the final weightlessness rate is 14.4%. CDs have been reported to decompose and lose weight at high temperature, especially for the CDs with low crystallinity.[44,45] The same results were also

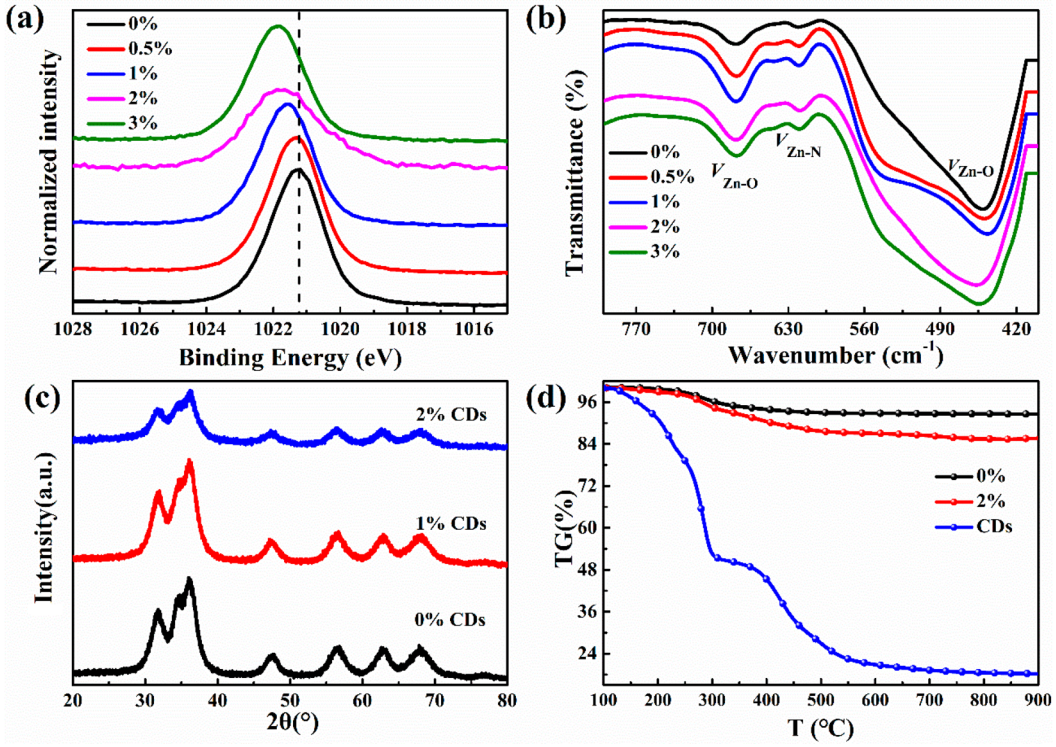

Figure 4. (a) Zn $2p^{3/2}$ XPS, (b) FT-IR spectra, and (c) XRD patterns of ZnO and CD@ZnO. (d) TG curves of ZnO and CD@ZnO (2%) nanoparticles.

https://dx.doi.org/10.1021/acsaem.0c02323
ACS Appl. Energy Mater. 2020, 3, 11388−11397

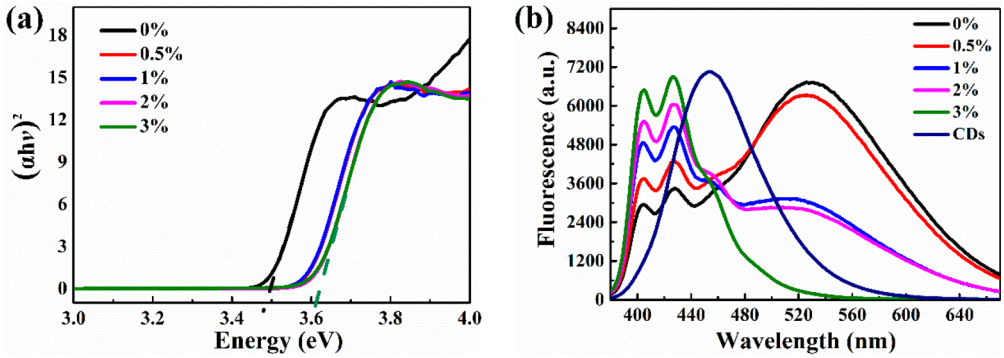

Figure 5. (a) $(\alpha h\nu)^2$ versus $h\nu$ and (b) PL spectra of ZnO, CDs, and CD@ZnO (excitation at 330 nm).

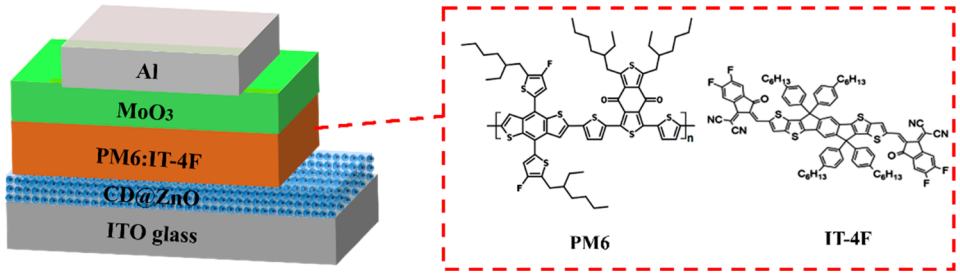

Figure 6. Structure diagram of PSCs and molecular structures of PM6 and IT-4F.

observed in our experiments (Figure 4d). It can be seen that the synthesized CDs have two rapid weight losses at 250 and 400 °C, which may be related to the decomposition of their surface functional groups. Finally, the weight loss of CDs reaches 80% at 550 °C and remains unchanged. Therefore, it can be inferred that CD@ZnO with higher weightlessness rate is mainly due to the lower thermal stability of CDs in composite nanoparticles, which further confirms the introduction of CDs into CD@ZnO nanoparticles. According to TG results, the CD@ZnO nanoparticles consists of 85.6 wt % ZnO, 7.0 wt % CDs, and 7.4 wt % impurities. It can be clearly seen that the CD@ZnO doped with 2 wt % CDs has a weight loss of 7 wt %, which is much greater than the doping ratio of CDs. This is mainly because the doping ratio of CDs is calculated based on the assumption that the ZnO yield is 100%, but the synthesis process of ZnO must have materials loss, and the yield must be less than 100%. In addition, there are some unreacted impurities in the product. These factors ultimately lead to the fact that the ratio of CDs in CD@ZnO is higher than the original calculated value.

The optical properties of the samples were further characterized and analyzed. Figure S2 displays the UV−vis absorption spectra of pristine ZnO and CD@ZnO with different doping ratio of CDs. As seen here, the absorption cutoff edge of pristine ZnO is at 360 nm, while that of CD@ZnO has a significant blue shift (to 351 nm). It can be seen from Figure S3 that the CDs has a strong absorption at 370 nm, but the absorption cutoff edge of CD@ZnO has blue-shifted to 351 nm, which indicates that the absorption of CD@ZnO is not affected by the absorption of CDs. As we all know, the UV−vis absorption spectrum of nanoparticles is related to their particle size, and the absorption cutoff edge of the sample will move to the shortwave direction as the particle size decreases, resulting in a blue shift effect.[46] TEM results (Figure 3a) prove that the CD@ZnO is a core−shell structured nanoparticle, so the introduction of CDs makes the ZnO shell thinner (Figure 4c). Therefore, it is speculated that the thinning of the ZnO shell may be the main reason for the blue shift in the UV−vis of CD@ZnO. According to the Tauc plot,[47] the energy band gaps (E_g) of pristine ZnO and CD@ZnO can be calculated. As can be seen in Figure 5a, the E_g of pristine ZnO is 3.48 eV, while that of CD@ZnO increases with the increase of CDs doping ratio. With the doping of 3% CDs, the E_g of CD@ZnO increases to 3.61 eV.

Figure 5b shows that under 330 nm excitation, both ZnO and CD@ZnO exhibit three PL emission bands. It is reported that the emission peaks at 408 and 426 nm are corresponding to the radiation annihilation of excitons on ZnO conductive tape,[48] while the emission band around at 530 nm can be attributed to the defect emission.[49,50] It is noteworthy that the introduction of CDs enhances the PL emission of CD@ZnO at 408 and 426 nm, while the PL emission peak of CD is located at 460 nm, which indicates that the enhancement of PL emission of CD@ZnO has nothing to do with the PL emission of CDs. Numerous studies have proved that the enhancement of blue fluorescence emission of ZnO is related to the increase of its crystallinity,[51,52] so we speculate that the introduced CDs induce the growth of ZnO crystals and improve their crystallization. Moreover, the charge transfer between CDs and ZnO may be another factor leading to the enhanced blue emission of CD@ZnO. In addition, CD@ZnO exhibits strong blue fluorescence emission, which makes it very promising for blue fluorescent materials in LED devices. Also, it can be clearly seen that the introduction of CDs decreases the defects peak around 530 nm, suggesting the CDs effectively inhibit the defects of ZnO, thus improving the electrical properties. The same phenomenon was also found on ZnO nanocrystalline film passivated by dodecanethiol and ethanedithiol.[53,54] The passivation mechanism for CDs is believed to be related to the reduction of oxygen vacancies, which is achieved by the formation of the Zn−N and Zn−O−C bonding on the ZnO surface.[55] In addition, electrons can transfer across the Zn−N

https://dx.doi.org/10.1021/acsaem.0c02323
ACS Appl. Energy Mater. 2020, 3, 11388−11397

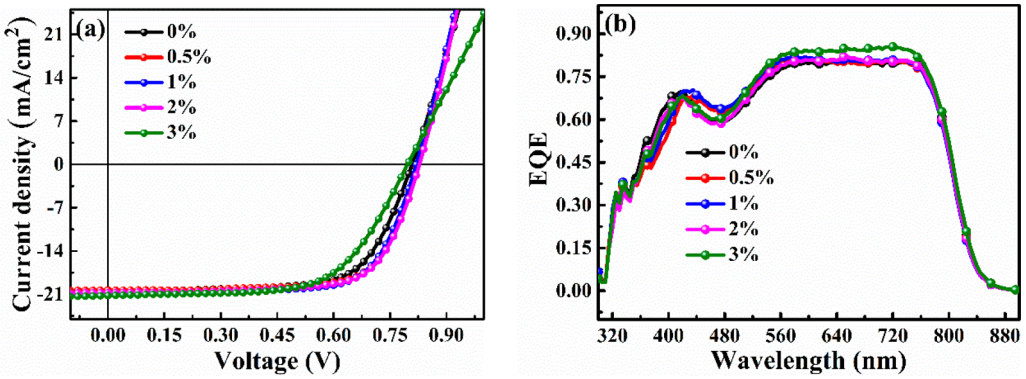

Figure 7. (a) $J-V$ curves and (b) EQE spectra of PSCs based on different ETLs.

Table 1. Device Parameters of PM6:IT-4F PSCs with Different ETL

m(CDs):m(ZnO) (%)	V_{OC} (V)	J_{SC} (mA/cm^2)	FF	PCE (%) (av PCE ± SD)
0	0.81	20.44	0.68	11.26 (11.17 ± 0.02)
0.5	0.82	20.32	0.72	12.00 (11.54 ± 0.06)
1	0.82	20.90	0.70	12.01 (12.01 ± 0.01)
2	0.83	20.75	0.71	12.23 (11.94 ± 0.03)
3	0.80	21.21	0.63	10.69 (10.62 ± 0.00)

bonding, thereby increasing the exciton lifetime, which will also improve the electrical properties of CD@ZnO.

The colloidal stability of CD@ZnO ink is of great significance for its application in PSCs. The ζ potential is often used to characterize the colloidal stability of solutions, and its absolute value has a positive correlation with colloidal stability. Figure S4 summarized the ζ potential data of ZnO and CD@ZnO. The ζ potential of as-prepared ZnO nanoparticles is +45 mV. With different doping concentration of CDs, CD@ZnO shows an increase of ζ potential, indicating that the introduction of CDs improves the colloidal stability of ZnO, as can be confirmed with previous HRTEM observations (Figure 2). The improvement in colloidal stability of CD@ZnO not only improves both the storage time but the film-forming quality.

3.2. CD@ZnO as ETLs of PSCs. To evaluate the feasibility of CD@ZnO as ETL in PSCs, PSCs based on CD@ZnO ETL were fabricated and characterized. The structural formula of PM6 and IT-4F and device configuration are shown in Figure 6. The $J-V$ curves of the non-fullerene PSCs with different ETLs (ZnO and CD@ZnO) are illustrated in Figure 7a, and the related parameters are listed in Table 1. With pristine ZnO as ETL, the PSC achieves a PCE of 11.26%, of which the V_{OC} is 0.81 V, J_{SC} is 20.44 mA/cm^2, and FF is 0.68, which indicates that the device performance basically reached the level reported in previous literature.[56] When using CD@ZnO instead of ZnO as ETLs, the inverted PSCs exhibit enhanced PCE. Among them, the PCE of the solar cell with CD@ZnO (2%) ETL shows the highest PCE of 12.23%, in which the V_{OC} is 0.83 V, J_{SC} is 20.75 mA/cm^2, and FF is 0.71. In addition, Figure 7b shows the EQE spectra of the inverted PSCs based on ZnO and CD@ZnO as ETLs. Compared with ETL using only ZnO, devices with CD@ZnO as ETLs exhibit slightly enhanced absorption in the 400−750 nm range, so the J_{SC} of PSCs based CD@ZnO ETL has increased, which may be because the use of CD@ZnO ETL increased charge utilization of the donor materials.

In order to confirm the best effect when CDs doping content is 2%, a series of repeated experiments have been done to eliminate unexpected experiment errors, and the results are summarized in the standard box plot, as shown in Figure S5. As a result, the average V_{OC}, J_{SC}, and FF of PSCs with CD@ZnO (0.5−2%) ETLs are all higher than those of pristine ZnO-based ones. The result means the devices have excellent photoelectric properties and good reproducibility with CD@ZnO as ETLs. The improvement in V_{OC}, J_{SC}, FF eventually leads to the improvement in device PCE, achieving the best effect when the CDs doping is 2%.

At present, the active layer systems commonly used in PSCs can be divided into two categories; one is the fullerene system, and the other is the non-fullerene system. Generally speaking, non-fullerene has higher PCE than fullerene system. PM6:IT-4F, as the representative of non-fullerene system, has demonstrated that the device PCE using CD@ZnO as ETL is significantly higher than that using pristine ZnO as ETL. In order to verify whether CD@ZnO ETL can also improve the PCE of fullerene based PSCs, PSCs with P3HT:bis-PCBM as active layer based on different ETLs were prepared and characterized, as shown in Figure S6 and Table S1. The results show that the parameters of PSCs including V_{OC}, J_{SC}, and FF are greatly improved by using CD@ZnO as ETLs. The CD@ZnO (1%) based PSC achieves the highest PCE of 4.64%, which is 12% higher than that of the PSCs with pristine ZnO as ETL. In summary, CD@ZnO can be widely applied in fullerene- and non-fullerene-based PSCs to give better performance than pristine ZnO-based PSCs.

As can be seen from Table 1, Table S1, and Figure S5, the performance improvement of the PSCs with CD@ZnO ETLs can be mostly attributed to the enhancement in V_{OC} and FF. In general, the V_{OC} of the PSCs is mainly determined by the matching degree between the lowest unoccupied molecular orbital (LUMO) energy level of the acceptor and the highest occupied molecular orbital (HOMO) energy level of the donor. However, V_{OC} can also be affected by the work function (WF) between the cathode and anode interface layer; moreover, a mismatched WF can decrease the V_{OC} of device.[57] In order to explore the relationship between WF of CD@ZnO and the V_{OC} of PSCs, the UPS data about pristine ZnO and

https://dx.doi.org/10.1021/acsaem.0c02323
ACS Appl. Energy Mater. 2020, 3, 11388−11397

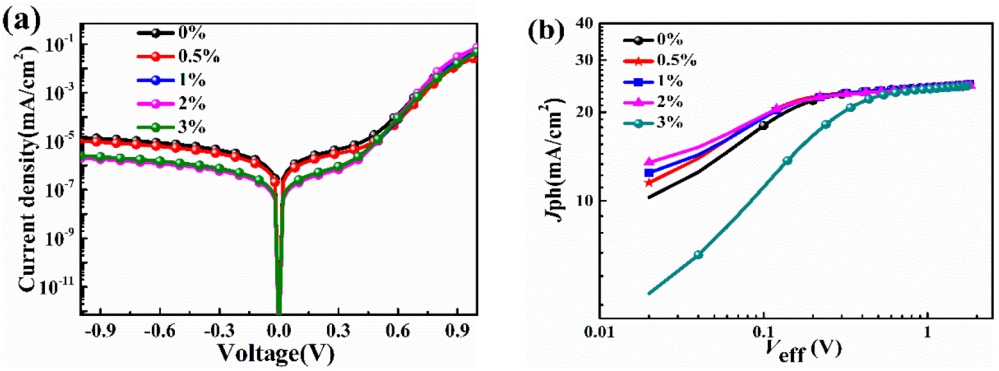

Figure 8. (a) $J-V$ curves of PSCs based on different ETLs in the dark condition. (b) $J_{ph}-V_{eff}$ curves of PSCs based on different ETLs in 100 mW/cm^2 AM 1.5G illumination.

CD@ZnO were tested, which has been given in Figure S7a and Figure S7b). The cutoff edge of kinetic energy and abscissa can be used to further determine the value of WF, which have been discussed by Braun et al.[58] It can be seen that the CD@ZnO has a lower WF (3.92−4.01 eV) than pristine ZnO (4.04 eV), which enhances the electric field driving force in the device and reduces the charge barrier at the interface of active layer and cathode, resulting in higher V_{OC} of PSCs.[25]

As we all know, in the dark environment, the $J-V$ curves of PSCs can simulate diode properties. Figure 8a shows the dark $J-V$ curves of the PSCs based on different ETLs. For an ideal p−n junction solar cell, according to literature that has been reported,[59] the dark $J-V$ curve can be fitted by the following eq 1:[60]

$$J = J_0\left\{\exp\left[\frac{q(V - JR_{sh})}{nk_BT}\right] - 1\right\} + \frac{V - JR_s}{R_{sh}} - J_{ph} \quad (1)$$

where J_0, q, n, R_s, R_{sh} represent the reverse saturation current density, elementary charge, the ideal factor of diode, the series resistance, and shunt resistance of PSCs, while k_B, T, and J_{ph} represent Boltzmann constant, absolute temperature, and photogenerated current density, respectively. In the dark environment, the photogenerated current density of PSCs is 0 (J_{ph} = 0). Equation 1 was used to fit the curves of PSCs,[61,62] and the results of curve fitting are shown in Figure S8. These devices all show good diode characteristics, and the key parameters of PSCs fitting are summarized in Table 2. As we can see, the PSCs with CD@ZnO (0.5%, 1%, 2%) as ETL have lower value of J_0, n, and R_s and greater R_{sh} as to the PSCs using pristine ZnO as ETL. The lower J_0 of CD@ZnO-based devices confirms that CD@ZnO films have stronger charge extraction and block barriers properties.[61] In addition, it is known that the lower the n value is, the closer the device is to ideal diode properties. As can be seen in Table 2, the n value (<1.84) of PSCs using CD@ZnO (0.5%, 1%, 2%) as ETL is lower than that of pristine ZnO-based device(1.94), indicating less charge recombination at CD@ZnO ETL interface. Furthermore, the devices using CD@ZnO (0.5%, 1%, 2%) as ETLs show lower R_s and higher R_{sh}, which not only implies the active layer and CD@ZnO form better ohmic contact but also obviously suppressed defects of ZnO. From these data, it can be concluded that CD@ZnO (0.5%, 1%, 2%) ETLs decrease the charge-carrier recombination and increase the carrier selectivity at the interface of the active layer and cathode, resulting in enhanced device performance.

Table 2. Key Fitting Parameters of PSCs Based on Different ETLs

entry	J_0 (A/cm^2)	n	R_s (Ω cm^2)	R_{sh} (Ω cm^2)
pristine ZnO	4.50×10^{-10}	1.90	2.5	7.40×10^4
0.5%	2.00×10^{-10}	1.84	2.4	9.80×10^4
1%	1.50×10^{-10}	1.76	2.3	4.00×10^5
2%	1.00×10^{-10}	1.68	2.3	5.00×10^5
3%	3.00×10^{-10}	1.84	3.5	4.00×10^5

Furthermore, the relationship between the photocurrent density (J_{ph}) and effective voltage (V_{eff}) of PSCs with different ETL was also tested, and the results are given in Figure 8b, where $J_{ph} = J_L - J_D$ (J_L and J_D represent the current density in illumination (Figure 7a) and dark (Figure 8a) conditions, respectively), while $V_{eff} = V_0 - V$ (where V_0 represents the voltage at J_{ph} = 0 and V represents the applied voltage).[63] When V_{eff} is high enough, J_{ph} can be saturated and the current density is called $J_{ph,sat}$. The probability of exciton dissociation and charge transport can be estimated using $J_{ph}/J_{ph,sat}$. In short-circuit current and maximum output power conditions, J_{ph} is called $J_{ph,sc}$ and $J_{ph,max}$, respectively. The ratios of $J_{ph,sc}/J_{ph,sat}$ and $J_{ph,max}/J_{ph,sat}$ are calculated and listed in Table 3. The $J_{ph,sc}/J_{ph,sat}$ ratio for using CD@ZnO-based devices (97.1%, 97.1%, 97.2% for 0.5%, 1%, 2% CDs, respectively) is slightly higher than that of devices (97.1%) with pristine ZnO as ETLs, which indicates that the CD@ZnO-based PSCs have better exciton dissociation. Moreover, the PSCs with CD@ZnO as ETLs also show a higher $J_{ph,max}/J_{ph,sat}$ ratio (88.5%, 88.8%, 89.6% for 0.5%, 1%, 2% CDs, respectively) than PSCs with pristine ZnO (84.3%) under maximum power output conditions, indicating that the charge extraction and collection are enhanced in PSCs with CD@ZnO (0.5%, 1%, 2%) as ETLs.[64] Therefore, it is believed that the better photovoltaic performance of PSCs based on CD@ZnO (0.5%, 1%, 2%) is due to the promotion in charge

Table 3. Key Parameters of the PSCs under the Conditions of Short-Circuit Current and Maximum Output Power According to $J_{ph}-V_{eff}$ Curves

entry	$J_{ph,sc}/J_{ph,sat}$	$J_{ph,max}/J_{ph,sat}$
pristine ZnO	97.1%	84.3%
0.5%	97.1%	88.5%
1%	97.1%	88.8%
2%	97.2%	89.6%
3%	96.3%	77%

https://dx.doi.org/10.1021/acsaem.0c02323
ACS Appl. Energy Mater. 2020, 3, 11388−11397

extraction and reduction in exciton recombination between active layers and the cathode layer.

4. CONCLUSION

The performance of PSCs is improved by using a novel core−shell structure of CD@ZnO nanoparticles as ETL. During the synthesis of CD@ZnO, CDs are introduced and coated with ZnO, which can be confirmed from the characterization results of HRTEM, EDX, and XPS. The introduced CD induces and participates in the growth of the ZnO crystal, which improves the monodispersity of CD@ZnO, increases its band gap, and effectively suppresses its surface defects. Therefore, CD@ZnO contributes to the enhanced charge separation and extraction and reduced charge recombination at the active layer/ETL interface of PSCs, consequently accounting for enhanced V_{OC} and FF. As a result, PCE up to 12.23% is achieved for the device with PM6:IT-4F as active layer and CD@ZnO as ETL, which shows over 8.61% enhancement with respect to the referential device based on pristine ZnO (11.26%). In addition, PCE improvement is also observed in fullerene-based solar cell with P3HT:bis-PCBM as active layer and CD@ZnO as ETL. This work highlights the promising potential of solution-processable CD@ZnO nanoparticles in fabricating highly efficient PSCs and also provides a new strategy for passivating the defects of metal oxide.

■ ASSOCIATED CONTENT

Supporting Information

The Supporting Information is available free of charge at https://pubs.acs.org/doi/10.1021/acsaem.0c02323.

Figures S1−S9 and Table S1 regrading the XPS spectra, UV−vis absorption, ζ potential, device performance statistical data, UPS spectra of ZnO and CD@ZnO; $J-V$ curves, EQE spectra, simulated dark $J-V$ curves, degradation curves, and energy level diagram of polymer solar cells (PDF)

■ AUTHOR INFORMATION

Corresponding Authors

Lingpeng Yan − *Key Laboratory of Interface Science and Engineering in Advanced Materials, Ministry of Education and Institute of New Carbon Materials, Taiyuan University of Technology, Taiyuan 030024, P. R. China; Printed Electronics Research Center, Suzhou Institute of Nano-Tech and Nano-Bionics, Chinese Academy of Sciences, Suzhou 215123, P. R. China*; Phone: +86-512-6287-2769; Email: lpyan2014@sinano.ac.cn

Yongzhen Yang − *Key Laboratory of Interface Science and Engineering in Advanced Materials, Ministry of Education, Taiyuan University of Technology, Taiyuan 030024, P. R. China*; orcid.org/0000-0003-0566-4802; Phone: +86-0351-6014138; Email: yyztyut@126.com

Chang-Qi Ma − *Printed Electronics Research Center, Suzhou Institute of Nano-Tech and Nano-Bionics, Chinese Academy of Sciences, Suzhou 215123, P. R. China*; orcid.org/0000-0002-9293-5027; Phone: +86-512-6287-2769; Email: cqma2011@sinano.ac.cn

Authors

Wensheng Zhao − *Key Laboratory of Interface Science and Engineering in Advanced Materials, Ministry of Education, Taiyuan University of Technology, Taiyuan 030024, P. R. China; Printed Electronics Research Center, Suzhou Institute of Nano-Tech and Nano-Bionics, Chinese Academy of Sciences, Suzhou 215123, P. R. China*

Huimin Gu − *Key Laboratory of Interface Science and Engineering in Advanced Materials, Ministry of Education, Taiyuan University of Technology, Taiyuan 030024, P. R. China; Printed Electronics Research Center, Suzhou Institute of Nano-Tech and Nano-Bionics, Chinese Academy of Sciences, Suzhou 215123, P. R. China*

Zerui Li − *Printed Electronics Research Center, Suzhou Institute of Nano-Tech and Nano-Bionics, Chinese Academy of Sciences, Suzhou 215123, P. R. China*

Yaling Wang − *School of Energy and Power Engineering, North University of China, Taiyuan 030051, P. R. China*

Qun Luo − *Printed Electronics Research Center, Suzhou Institute of Nano-Tech and Nano-Bionics, Chinese Academy of Sciences, Suzhou 215123, P. R. China*; orcid.org/0000-0002-7527-460X

Xuguang Liu − *Institute of New Carbon Materials, Taiyuan University of Technology, Taiyuan 030024, P. R. China*

Hua Wang − *Key Laboratory of Interface Science and Engineering in Advanced Materials, Ministry of Education and College of Textile Engineering, Taiyuan University of Technology, Taiyuan 030024, P. R. China*; orcid.org/0000-0002-2976-9521

Complete contact information is available at: https://pubs.acs.org/10.1021/acsaem.0c02323

Notes

The authors declare no competing financial interest.

■ ACKNOWLEDGMENTS

The authors acknowledge the financial support from the Ministry of Science and Technology of China (Grant 2016YFA0200700), Chinese Academy of Science (Grants YJKYYQ20180029 and CAS-ITRI 2019010), National Natural Science Foundation of China (Grants 61904121 and 51773224), Youth Innovation Promotion Association, CAS (Grant 2019317), Natural Science Foundation of Shanxi Province (Grants 201801D221136 and 201901D211282), and Science Foundation of North University of China (Grant XJJ201925). Thanks are also given for the support of Suzhou Vacuum Interconnected Nanotechnology Workstation H005-2019 project.

■ REFERENCES

(1) Holliday, S.; Li, Y. L.; Luscombe, C. K. Recent Advances in High Performance Donor-Acceptor Polymers for Organic Photovoltaics. *Prog. Polym. Sci.* **2017**, *70*, 34−51.

(2) Liu, Q.; Jiang, Y.; Jin, K.; Qin, J.; Xu, J.; Li, W.; Xiong, J.; Liu, J.; Xiao, Z.; Sun, K.; Yang, S.; Zhang, X.; Ding, L. 18% Efficiency Organic Solar Cells. *Sci. Bull.* **2020**, *65*, 272−275.

(3) Wang, G.; Melkonyan, F. S.; Facchetti, A.; Marks, T. J. All-Polymer Solar Cells: Recent Progress, Challenges, and Prospects. *Angew. Chem., Int. Ed.* **2019**, *58*, 4129−4142.

(4) Yin, Z. G.; Wei, J. J.; Zheng, Q. D. Interfacial Materials for Organic Solar Cells: Recent Advances and Perspectives. *Adv. Sci.* **2016**, *3*, 1500362.

(5) Angelini, G.; De Maria, P.; Fontana, A.; Pierini, M.; Maggini, M.; Gasparrini, F.; Zappia, G. Study of the Aggregation Properties of a Novel Amphiphilic C60 Fullerene Derivative. *Langmuir* **2001**, *17*, 6404−6407.

(6) Huang, J.; Yin, Z. G.; Zheng, Q. D. Applications of ZnO in Organic and Hybrid Solar Cells. *Energy Environ. Sci.* **2011**, *4*, 3861−3877.
(7) Kyaw, A. K. K.; Wang, D. H.; Wynands, D.; Zhang, J.; Nguyen, T. Q.; Bazan, G. C.; Heeger, A. J. Improved Light Harvesting and Improved Efficiency by Insertion of an Optical Spacer (ZnO) in Solution-Processed Small-Molecule Solar Cells. *Nano Lett.* **2013**, *13*, 3796−3801.
(8) Kyaw, A. K. K.; Sun, X. W.; Jiang, C. Y.; Lo, G. Q.; Zhao, D. W.; Kwong, D. L. An Inverted Organic Solar Cell Employing a Sol-Gel Derived ZnO Electron Selective Layer and Thermal Evaporated MoO_3 Hole Selective Layer. *Appl. Phys. Lett.* **2008**, *93*, 221107.
(9) Beek, W. J. E.; Wienk, M. M.; Kemerink, M.; Yang, X. N.; Janssen, R. A. J. Hybrid Zinc Oxide Conjugated Polymer Bulk Heterojunction Solar Cells. *J. Phys. Chem. B* **2005**, *109*, 9505−9516.
(10) Yang, B.; Bai, Y. M.; Zeng, R.; Zhao, C. Y.; Zhang, B.; Wang, J.; Hayat, T. S. W. R.; Alsaedi, A. M.; Tan, Z. A. Low-Temperature in-Situ Preparation of ZnO Electron Extraction Layer for Efficient Inverted Polymer Solar Cells. *Org. Electron.* **2019**, *74*, 82−88.
(11) Wen, X. B.; Fang, S. M.; Xu, Y. C.; Zheng, N.; Liu, L. L.; Xie, Z. Q.; Wurthner, F. Enhanced Electron Transportation by Dye Doping in Very Low-Temperature (< 130 °C)-Processed Sol-Gel ZnO toward Flexible Organic Solar Cells. *ACS Appl. Mater. Interfaces* **2019**, *11*, 34151−34157.
(12) Trost, S.; Zilberberg, K.; Behrendt, A.; Polywka, A.; Gorrn, P.; Reckers, P.; Maibach, J.; Mayer, T.; Riedl, T. Overcoming the "Light-Soaking" Issue in Inverted Organic Solar Cells by the Use of Al:ZnO Electron Extraction Layers. *Adv. Energy Mater.* **2013**, *3*, 1437−1444.
(13) Wu, N.; Luo, Q.; Bao, Z. M.; Lin, J.; Li, Y. Q.; Ma, C. Q. Zinc Oxide: Conjugated Polymer Nanocomposite as Cathode Buffer Layer for Solution Processed Inverted Organic Solar Cells. *Sol. Energy Mater. Sol. Cells* **2015**, *141*, 248−259.
(14) Li, J. S.; Jian, H. M.; Yao, L. L.; Zhao, M.; Shu, J.; Xiao, X. W.; Jiu, T. G. Highly Efficient Regular Polymer Solar Cells Based on Li-TFSI Doping ZnO as Electron-Transporting Interlayers. *Sol. Energy* **2018**, *169*, 49−54.
(15) Cheng, Y. S.; Liao, S. H.; Li, Y. L.; Chen, S. A. Physically Adsorbed Fullerene Layer on Positively Charged Sites on Zinc Oxide Cathode Affords Efficiency Enhancement in Inverted Polymer Solar Cell. *ACS Appl. Mater. Interfaces* **2013**, *5*, 6665−6671.
(16) Datt, R.; Bishnoi, S.; Gupta, R.; Haranath, D.; Sharma, S. N.; Gupta, G.; Arya, S.; Kumar, S.; Gupta, V. Dual-Functional Cathode Buffer Layer for Power Conversion Efficiency Enhancement of Bulk-Heterojunction Solar Cells. *Synth. Met.* **2019**, *255*, 116112.
(17) Rasool, S.; Doan, V. V.; Lee, H. K.; Lee, S. K.; Lee, J. C.; Moon, S. J.; So, W. W.; Song, C. E.; Shin, W. S. Enhanced Photostability in Polymer Solar Cells Achieved with Modified Electron Transport Layer. *Thin Solid Films* **2019**, *669*, 42−48.
(18) Wei, J. F.; Ji, G. Q.; Zhang, C. J.; Yan, L. P.; Luo, Q.; Wang, C.; Chen, Q.; Yang, J. L.; Chen, L. W.; Ma, C. Q. Silane-Capped ZnO Nanoparticles for Use as the Electron Transport Layer in Inverted Organic Solar Cells. *ACS Nano* **2018**, *12*, 5518−5529.
(19) Zhu, X. Q.; Guo, B.; Fang, J.; Zhai, T. S.; Wang, Y. N.; Li, G. W.; Zhang, J. Q.; Wei, Z. X.; Duhm, S.; Guo, X.; Zhang, M. J.; Li, Y. F. Surface Modification of ZnO Electron Transport Layers with Glycine for Efficient Inverted Non-Fullerene Polymer Solar Cells. *Org. Electron.* **2019**, *70*, 25−31.
(20) Hu, L.; Chen, L.; Hu, X. T.; Chen, Y. W. Solution Processed and Self-Assembled Polymerizable Fullerenes/Metal Oxide as an Interlayer for High Efficient Inverted Polymer Solar Cells. *J. Mater. Chem. C* **2014**, *2*, 10282−10290.
(21) Ling, Z. T.; Zhao, Y.; Wang, S. L.; Pan, S. H.; Lian, H.; Peng, C. Y.; Yang, X. Y.; Liao, Y. J.; Lan, W. X.; Wei, B.; Chen, G. High-Performance Light-Soaking-Free Polymer Solar Cells Based on a LiF Modified ZnO Electron Extraction Layer. *J. Mater. Chem. C* **2019**, *7*, 9354−9361.
(22) Zhang, Q. N.; Peng, R. Z.; Zhang, C. F.; Chen, D. Z.; Lin, Z. H.; Chang, J. J.; Zhang, J. C.; Hao, Y. Inverted Organic Solar Cells with Low-Temperature Al-Doped-ZnO Electron Transport Layer Processed from Aqueous Solution. *Polymers* **2018**, *10*, 127.
(23) Park, S.; Kang, R.; Cho, S. Effect of an Al-Doped ZnO Electron Transport Layer on the Efficiency of Inverted Bulk Heterojunction Solar Cells. *Curr. Appl. Phys.* **2020**, *20*, 172−177.
(24) Lin, Z. H.; Chang, J. J.; Zhang, C. F.; Zhang, J. C.; Wu, J. S.; Hao, Y. Low Temperature Aqueous Solution-Processed Li Doped ZnO Buffer Layers for High Performance Inverted Organic Solar Cells. *J. Mater. Chem. C* **2016**, *4*, 6169−6175.
(25) Chen, G.; Wang, T. H.; Li, C. Y.; Yang, L. Q.; Xu, T.; Zhu, W. Q.; Gao, Y. L.; Wei, B. Enhanced Photovoltaic Performance in Inverted Polymer Solar Cells Using Li Ion Doped ZnO Cathode Buffer Layer. *Org. Electron.* **2016**, *36*, 50−56.
(26) Shin, K. S.; Lee, K. H.; Lee, H. H.; Choi, D.; Kim, S. W. Enhanced Power Conversion Efficiency of Inverted Organic Solar Cells with a Ga-Doped ZnO Nanostructured Thin Film Prepared Using Aqueous Solution. *J. Phys. Chem. C* **2010**, *114*, 15782−15785.
(27) Wei, J. J.; Yin, Z. G.; Chen, S. C.; Zheng, Q. D. Low-Temperature Solution-Processed Zinc Tin Oxide Film as a Cathode Interlayer for Organic Solar Cells. *ACS Appl. Mater. Interfaces* **2017**, *9*, 6186−6193.
(28) Peng, H.; Xu, W. P.; Zhou, F.; Zhang, J.; Li, C. N. Enhanced Efficiency of Inverted Polymer Solar Cells Using Surface Modified Cs-Doped ZnO as Electron Transporting Layer. *Synth. Met.* **2015**, *205*, 164−168.
(29) Lin, X. F.; Yang, Y. Z.; Nian, L.; Su, H.; Ou, J. M.; Yuan, Z. K.; Xie, F. Y.; Hong, W.; Yu, D. S.; Zhang, M. Q.; Ma, Y. G.; Chen, X. D. Interfacial Modification Layers Based on Carbon Dots for Efficient Inverted Polymer Solar Cells Exceeding 10% Power Conversion Efficiency. *Nano Energy* **2016**, *26*, 216−223.
(30) Zhang, R. Q.; Zhao, M.; Wang, Z. Q.; Wang, Z. T.; Zhao, B.; Miao, Y. Q.; Zhou, Y. J.; Wang, H.; Hao, Y. Y.; Chen, G.; Zhu, F. R. Solution-Processable ZnO/Carbon Quantum Dots Electron Extraction Layer for Highly Efficient Polymer Solar Cells. *ACS Appl. Mater. Interfaces* **2018**, *10*, 4895−4903.
(31) Wang, Y. L.; Yan, L. P.; Ji, G. Q.; Wang, C.; Gu, H. M.; Luo, Q.; Chen, Q.; Chen, L. W.; Yang, Y. Z.; Ma, C. Q.; Liu, X. G. Synthesis of N,S-Doped Carbon Quantum Dots for Use in Organic Solar Cells as the ZnO Modifier to Eliminate the Light-Soaking Effect. *ACS Appl. Mater. Interfaces* **2019**, *11*, 2243−2253.
(32) Wang, Y. F.; Hu, A. G. Carbon Quantum Dots: Synthesis, Properties and Applications. *J. Mater. Chem. C* **2014**, *2*, 6921−6939.
(33) Yan, L. P.; Yang, Y. Z.; Ma, C. Q.; Liu, X. G.; Wang, H.; Xu, B. S. Synthesis of Carbon Quantum Dots by Chemical Vapor Deposition Approach for Use in Polymer Solar Cell as the Electrode Buffer Layer. *Carbon* **2016**, *109*, 598−607.
(34) Juang, T. Y.; Kao, J. C.; Wang, J. C.; Hsu, S. Y.; Chen, C. P. Carbonized Bamboo-Derived Carbon Nanodots as Efficient Cathode Interfacial Layers in High-Performance Organic Photovoltaics. *Adv. Mater. Interfaces* **2018**, *5*, 1800031.
(35) Han, M.; Zhu, S. J.; Lu, S. Y.; Song, Y. B.; Feng, T. L.; Tao, S. Y.; Liu, J. J.; Yang, B. Recent Progress on the Photocatalysis of Carbon Dots: Classification, Mechanism and Applications. *Nano Today* **2018**, *19*, 201−218.
(36) Wang, Y. L.; Zhao, Y. Q.; Zhang, Y.; Zhang, F.; Feng, X. T.; Chen, L.; Yang, Y. Z.; Liu, X. G. A Single-Phase Heteroatom Doped Carbon Dot Phosphor toward White Light-Emitting Diodes. *RSC Adv.* **2016**, *6*, 38761−38768.
(37) Ou, R. X.; Chen, Y. C.; Lin, C. H.; Guo, T. F.; Wen, T. C. Efficient Inverted Polymer Solar Cells Via Pyridine-Based Organic Molecules as Interfacial Modification Layer on Sol-Gel Zinc Oxide Surface. *Org. Electron.* **2018**, *63*, 93−97.
(38) Liao, S. H.; Jhuo, H. J.; Cheng, Y. S.; Chen, S. A. Fullerene Derivative-Doped Zinc Oxide Nanofilm as the Cathode of Inverted Polymer Solar Cells with Low-Bandgap Polymer (PTB7-Th) for High Performance. *Adv. Mater.* **2013**, *25*, 4766−4771.
(39) Gao, D. Q.; Zhang, J.; Yang, G. J.; Zhang, J. L.; Shi, Z. H.; Qi, J.; Zhang, Z. H.; Xue, D. S. Ferromagnetism in ZnO Nanoparticles

https://dx.doi.org/10.1021/acsaem.0c02323
ACS Appl. Energy Mater. 2020, 3, 11388−11397

Induced by Doping of a Nonmagnetic Element: Al. *J. Phys. Chem. C* **2010**, *114*, 13477−13481.
(40) Bajju, G. D.; Kundan, S.; Kapahi, A.; Gupta, D. Synthesis and Spectroscopic Studies of Axially Ligated Zn(II)5,10,15,20-Meso-tetra(p-chlorophenyl)porphyrin with Oxygen and Nitrogen Donors. *J. Chem.* **2013**, *2013*, 1−14.
(41) Hillman, F.; Jeong, H. K. Linker-Doped Zeolitic Imidazolate Frameworks (ZIFs) and Their Ultrathin Membranes for Tunable Gas Separations. *ACS Appl. Mater. Interfaces* **2019**, *11*, 18377−18385.
(42) Sharma, R.; Alam, F.; Sharma, A. K.; Dutta, V.; Dhawan, S. K. ZnO Anchored Graphene Hydrophobic Nanocomposite-Based Bulk Heterojunction Solar Cells Showing Enhanced Short-Circuit Current. *J. Mater. Chem. C* **2014**, *2*, 8142−8151.
(43) Liu, S. Z.; Sun, H. Q.; Suvorova, A.; Wang, S. B. One-Pot Hydrothermal Synthesis of ZnO-Reduced Graphene Oxide Composites Using Zn Powders for Enhanced Photocatalysis. *Chem. Eng. J.* **2013**, *229*, 533−539.
(44) Li, X. M.; Zhang, S. L.; Kulinich, S. A.; Liu, Y. L.; Zeng, H. B. Engineering Surface States of Carbon Dots to Achieve Controllable Luminescence for Solid-Luminescent Composites and Sensitive Be^{2+} Detection. *Sci. Rep.* **2015**, *4*, 4976.
(45) Wang, J. L.; Zhang, F.; Wang, Y. L.; Yang, Y. Z.; Liu, X. G. Efficient Resistance Against Solid-State Quenching of Carbon Dots Towards White Light Emitting Diodes by Physical Embedding into Silica. *Carbon* **2018**, *126*, 426−436.
(46) Meulenkamp; Eric, A. Synthesis and Growth of ZnO Nanoparticles. *J. Phys. Chem. B* **1998**, *102*, 5566−5572.
(47) Goh, E. G.; Xu, X.; McCormick, P. G. Effect of Particle Size on the UV Absorbance of Zinc Oxide Nanoparticles. *Scr. Mater.* **2014**, *78*−*79*, 49−52.
(48) Schmidt-Mende, L.; MacManus-Driscoll, J. L. ZnO-Nanostructures, Defects, and Devices. *Mater. Today* **2007**, *10*, 40−48.
(49) Chen, S.; Small, C. E.; Amb, C. M.; Subbiah, J.; Lai, T. H.; Tsang, S. W.; Manders, J. R.; Reynolds, J. R.; So, F. Inverted Polymer Solar Cells with Reduced Interface Recombination. *Adv. Energy Mater.* **2012**, *2*, 1333−1337.
(50) Ischenko, V.; Polarz, S.; Grote, D.; Stavarache, V.; Fink, K.; Driess, M. Zinc Oxide Nanoparticles with Defects. *Adv. Funct. Mater.* **2005**, *15*, 1945−1954.
(51) Liu, J.; Xie, S. F.; Chen, Y. L.; Wang, X. Y.; Cheng, H. B.; Liu, F.; Yang, J. H. Homoepitaxial Regrowth Habits of ZnO Nanowire Arrays. *Nanoscale Res. Lett.* **2011**, *6*, 619.
(52) Shinde, S. S.; Shinde, P. S.; Sapkal, R. T.; Oh, Y. W.; Haranath, D.; Bhosale, C. H.; Rajpure, K. Y. Photoelectrocatalytic Degradation of Oxalic Acid by Spray Deposited Nanocrystalline Zinc Oxide Thin Films. *J. Alloys Compd.* **2012**, *538*, 237−243.
(53) Bai, S.; Jin, Y. Z.; Liang, X. Y.; Ye, Z. Z.; Wu, Z. W.; Sun, B. Q.; Ma, Z. F.; Tang, Z.; Wang, J. P.; Wurfel, U.; Gao, F.; Zhang, F. L. Ethanedithiol Treatment of Solution-Processed ZnO Thin Films: Controlling the Intragap States of Electron Transporting Interlayers for Efficient and Stable Inverted Organic Photovoltaics. *Adv. Energy Mater.* **2015**, *5*, 1401606.
(54) Garcia, M. A.; Merino, J. M.; Fernandez Pinel, E.; Quesada, A.; de la Venta, J.; Ruiz Gonzalez, M. L.; Castro, G. R.; Crespo, P.; Llopis, J.; Gonzalez-Calbet, J. M.; Hernando, A. Magnetic Properties of ZnO Nanoparticles. *Nano Lett.* **2007**, *7*, 1489−1494.
(55) Jayalakshmi, G.; Saravanan, K.; Balasubramanian, T. Impact of Thiol and Amine Functionalization on Photoluminescence Properties of ZnO Films. *J. Lumin.* **2013**, *140*, 21−25.
(56) Cheng, H. W.; Raghunath, P.; Wang, K. L.; Cheng, P.; Haung, T. Y.; Wu, Q. T.; Yuan, J.; Lin, Y. C.; Wang, H. C.; Zou, Y. P.; Wang, Z. K.; Lin, M. C.; Wei, K. H.; Yang, Y. Potassium-Presenting Zinc Oxide Surfaces Induce Vertical Phase Separation in Fullerene-Free Organic Photovoltaics. *Nano Lett.* **2020**, *20*, 715−721.
(57) Brabec, C. J.; Shaheen, S. E.; Winder, C.; Sariciftci, N. S.; Denk, P. Effect of LiF/Metal Electrodes on the Performance of Plastic Solar Cells. *Appl. Phys. Lett.* **2002**, *80*, 1288−1290.
(58) Braun, S.; Salaneck, W. R.; Fahlman, M. Energy-Level Alignment at Organic/Metal and Organic/Organic Interfaces. *Adv. Mater.* **2009**, *21*, 1450−1472.
(59) Waldauf, C.; Scharber, M. C.; Schilinsky, P.; Hauch, J. A.; Brabec, C. J. Physics of Organic Bulk Heterojunction Devices for Photovoltaic Applications. *J. Appl. Phys.* **2006**, *99*, 104503.
(60) Qi, B. Y.; Wang, J. Z. Fill Factor in Organic Solar Cells. *Phys. Chem. Chem. Phys.* **2013**, *15*, 8972−8982.
(61) Zhang, H.; Stubhan, T.; Li, N.; Turbiez, M.; Matt, G. J.; Ameri, T.; Brabec, C. J. A Solution-Processed Barium Hydroxide Modified Aluminum Doped Zinc Oxide Layer for Highly Efficient Inverted Organic Solar Cells. *J. Mater. Chem. A* **2014**, *2*, 18917−18923.
(62) Lee, J. H.; Cho, S.; Roy, A.; Jung, H. T.; Heeger, A. J. Enhanced Diode Characteristics of Organic Solar Cells Using Titanium Suboxide Electron Transport Layer. *Appl. Phys. Lett.* **2010**, *96*, 163303.
(63) Cowan, S. R.; Street, R. A.; Cho, S. N.; Heeger, A. J. Transient Photoconductivity in Polymer Bulk Heterojunction Solar Cells: Competition between Sweep-out and Recombination. *Phys. Rev. B: Condens. Matter Mater. Phys.* **2011**, *83*, 035205.
(64) Chen, Y. C.; Wang, S.; Xue, L. W.; Zhang, Z. G.; Li, H. L.; Wu, L. X.; Wang, Y.; Li, F. H.; Zhang, F. L.; Li, Y. F. Insights into the Working Mechanism of Cathode Interlayers in Polymer Solar Cells Via $[(C_8H_{17})_4N]_4[SiW_{12}O_{40}]$. *J. Mater. Chem. A* **2016**, *4*, 19189−19196.

https://dx.doi.org/10.1021/acsaem.0c02323
ACS Appl. Energy Mater. 2020, 3, 11388−11397